PHYSICAL REVIEW FLUIDS **4**, 123603 (2019)

Role of extensional rheology on droplet bouncing

Min Y. Pack,[1,2] Angela Yang,[1,3] Antonio Perazzo,[1] Boyang Qin,[1] and Howard A. Stone[1,*]

[1]*Department of Mechanical and Aerospace Engineering, Princeton University, Princeton, New Jersey 08544, USA*

[2]*Department of Mechanical Engineering, Baylor University, Waco, Texas 76798, USA*

[3]*Department of Chemical Engineering, University of Southern California, Los Angeles, California 90089, USA*

(Received 7 June 2019; published 12 December 2019)

Recent experiments and theories have dismissed the role of increased extensional viscosity during impact of viscoelastic droplets. Here we show that for relatively low Weber numbers, $\mathrm{We} = \rho U_0^2 D_0/\gamma = O(10^0\text{–}10^1)$, where ρ is the density, U_0 the impact velocity, D_0 the droplet diameter, and γ the surface tension, droplets tend to bounce on an air film with a thickness, h, which sets off capillary waves that eventually focus into a single wave. This focusing causes rapid deformation of the droplet thus producing high strain rates, which we verified using a particle-tracking method. Without the addition of polymers, the capillary wave focusing generates droplet contact with the substrate; however, with the addition of polymers, contact is inhibited even for relatively small polymer concentrations (10 ppm). We attribute the inhibition of contact to the large increase in the extensional viscosity near the center of the droplet, which dissipates the kinetic energy of the droplet during impact and deformation.

DOI: 10.1103/PhysRevFluids.4.123603

I. INTRODUCTION

A mechanistic understanding of the dynamics of the impact of a non-Newtonian droplet is industrially relevant because of applications that include the deposition of agrochemicals [1], inkjet printing [2], spray coating [3], spray cooling [4], and spray drying [5]. In all of these cases, the degree with which the droplets contact neighboring droplets either in air or on a surface is critical to the success of each application. Impacting droplets have a range of dynamical regimes where they tend to deposit onto planar surfaces and splash at high speeds. Many studies have probed the interplay of the material properties of the droplet, ambient fluid, and the impacting surface (e.g., roughness, wettability, and the surrounding gas pressure) to determine the underlying physics [6–8].

While much work has been done on Newtonian fluids, less is known regarding the non-Newtonian effects on droplet impact with regard to how a droplet rebounds [9]. In particular, it has been reported that the addition of trace amounts of polymers (≈100 ppm, 4 MDa), such as poly(ethylene oxide) (PEO) in water, suppresses droplet rebounding on hydrophobic surfaces (e.g., a waxy leaf). The authors proposed that the response was due to the strong extensional viscosity increase during the droplet retraction phase in the bulk [10], which was later shown to be dominated by contact line dynamics [11]. The reason for the suppression of rebounding was attributed to contact line friction due to the polymer stretching and adhesion on the solid–liquid interface, which was the dominant factor and not the extensional viscosity increase in the droplet [11–13]. Bertola further argued that the extensional effects must be negligible in droplet bouncing since under

---

[*] Corresponding author: hastone@princeton.edu

Leidenfrost conditions (e.g., droplets bouncing on a layer of vapor at high temperatures), the PEO droplets [concentrations $O(100\ \text{ppm})$] bounced to even higher heights than pure water droplets [14]. During the spreading phase of the droplets on the vapor film, the maximum spreading diameter of the PEO droplet was similar for different polymer concentrations, and thus the stored elastic energy in the droplet presumably played a limited role. The explanation for the higher rebound heights was attributed to the decrease in the dissipated energy by the suppression of vorticity generation in the polymer-laden droplets during the droplet retraction phase.

The removal of the interstitial fluid (air in the examples above) is a prerequisite for contact of any object approaching a surface. Recent studies of drop impact have quantified the extant air film underneath a droplet, which can have a limiting thickness ∼1 μm at the center of the droplet moments prior to contact [15–20]. The relationship between the surrounding air and the droplet dynamics is complex. Under laboratory conditions, the droplets may bounce on air so there is no contact line to dissipate the energy [21–25] or even cause contact line instability postimpact well removed from the splash regime [26]. Nevertheless, the interaction of a non-Newtonian droplet with the surrounding gas is lacking in the literature although there are many non-Newtonian droplet impact studies to date, a majority of which focus on the spreading and bouncing dynamics without characterizing the ambient air film thicknesses upon impact [11,27–32].

Herein, we investigate the role of the polymer concentration on droplets bouncing on air. We visualize the impact dynamics of aqueous dilute PEO droplets (0–200 ppm, 4 MDa) on thin viscous silicone oil films ($\approx 10\,\mu\text{m}$ thick) by high-speed total internal reflection microscopy (TIRM). The thin film provides effectively a smooth surface which we have confirmed by direct visualization. In addition, particle-tracking velocimetry (PTV) is used to quantify the flow within the droplets. Based on our measurements, we argue that the large strain rates induce a large extensional viscosity near the middle of the droplet close to the substrate, which prevents the collapse of the top surface of the droplet over the underlying air film, thus allowing the droplets to bounce. This mechanism is distinct from that in Ref. [14] since our results are consistent with the bouncing being promoted during the spreading phase and not the retraction phase.

II. METHODOLOGY

To probe the air film between the droplet and the substrate with nanometer resolution, a thin viscous silicone oil film with thickness of $\approx 10\,\mu\text{m}$, which was verified by optical spectroscopy (Ocean Optics), was used to remove stochastic contact points caused by asperities on the glass slides [26,33]. The viscosity of the film was 10 000 cSt (Sigma-Aldrich). Based on the following observations, we assume that the oil film deformation has no dynamical influence on the droplet impact process. For instance, when we compare the air film shapes underneath droplets on solid surfaces to droplets on thin oil films, the profiles are similar for the corresponding Weber number, $\text{We} = \rho U_0^2 D_0/\gamma$, where ρ is the density, U_0 the impact velocity, D_0 the droplet diameter, and γ the surface tension [16,19]. The air film, h, between the oil film and the droplet was imaged using the TIRM technique [34] (Fig. 1), which resolves the spatiotemporal changes in the air film in three dimensions. The TIRM imaging setup revealed no film deformations during the impact process. The high-speed images were recorded using a Phantom 7.3 high-speed camera operating at 25 000 fps and 1 μs exposure time, which was connected to a Mitutoyo long-working distance 5 × objective (4.5 μm/pixel). The evanescent wave generated at the surface of the prism decays exponentially from the surface and is sensitive to the wavelength of the light (445 nm), incident angle of the light, and refractive indices of the substrate (silicone oil), air, and droplet [35].

Droplets with a diameter $D_0 \approx 2.2\,\text{mm}$ were formed by a blunt hypodermic needle connected to a syringe pump where the impact velocity, $U_0 \approx 0.24\text{–}1.5\,\text{m/s}$, was controlled by varying the release height. All experiments were conducted under ambient temperature of 23 °C. The droplet velocity and diameter were measured using a high-speed camera operating at 25 000 fps with a Sigma 105 mm macro lens (34 μm/pixel) illuminated by backlighting with a light-emitting diode or a laser sheet. The PEO concentration, c, in the droplets was varied between 0 and 200 ppm in

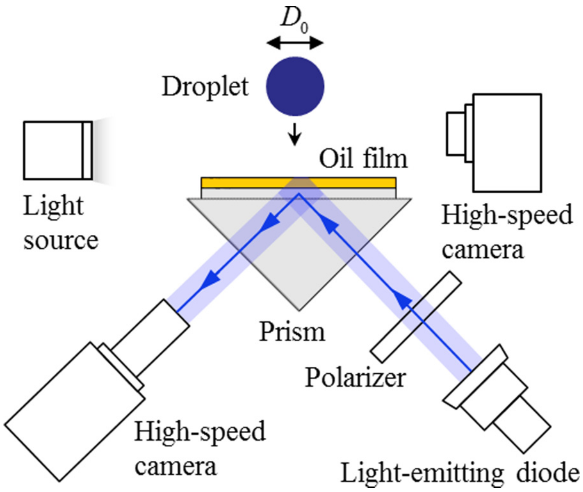

FIG. 1. Experimental schematic of the total internal reflection microscopy (TIRM) technique for studying droplet impact on a substrate.

water. The shear viscosity of the dilute PEO solutions was measured using a stress-controlled Anton Paar Physica MCR 301 rheometer using a double-gap spindle (shear rheology in the Supplemental Material [36]). For PEO with molecular weight of 4 MDa (4×10^6 g/mol), the critical overlap concentration $c^* \approx 567$ ppm.

We find that the extensional relaxation time, τ_E, a measure of viscoelasticity, is measureable for the 4 MDa PEO concentrations above $O(10$ ppm). One method for measuring the extensional relaxation time involves measuring the rate of thinning of a liquid thread during pinch off (Fig. 2). We use a standard experiment where a droplet neck initially thins due to the droplet weight and the corresponding thinning of the liquid thread is set by a balance of droplet inertia and the capillary

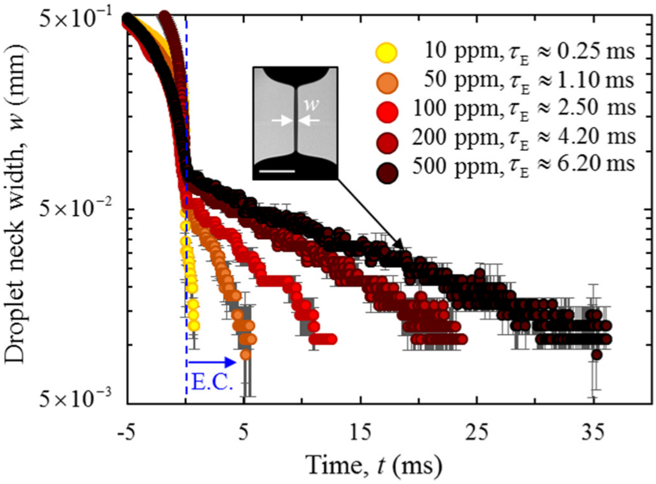

FIG. 2. Thinning dynamics of the droplet neck radius using the dripping-onto-substrate method [38]. Inset images show the minimum filament thickness at different times for 500 ppm PEO. The time origin ($t = 0$) is set at the boundary between the inertia-capillary and elasto-capillary regime, e.g., E.C. boundary. The error bars were determined from three independent experiments. The scale bar represents 1 mm.

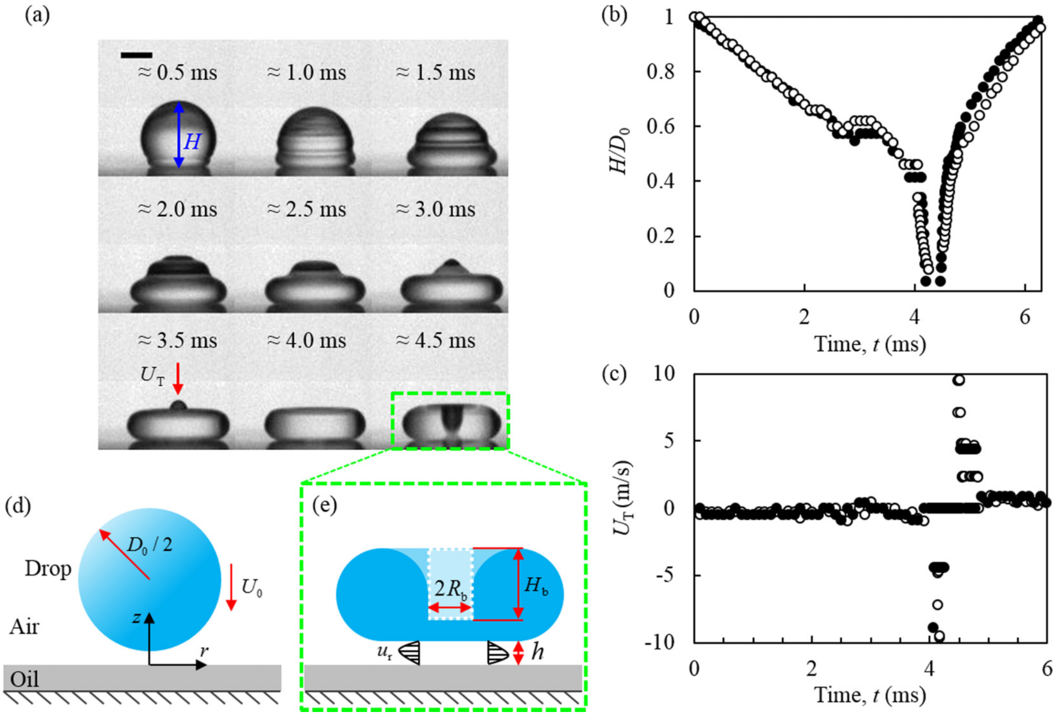

FIG. 3. (a) Droplet impact showing capillary wave propagation as a function of time. The red arrow indicates the final wave prior to the inversion of the droplet top surface, which occurs between 4 and 4.5 ms; We ≈ 5 and the scale bar represents 1 mm. (b) The distance of the top surface from the substrate, normalized by the droplet diameter, as a function of time. The open circles represent data from 100 ppm PEO droplets and the filled circles represent 10 ppm PEO droplets. Both droplets have We ≈ 5. (c) The change in the top surface velocity, U_T, with respect to time. (d) Schematic representation of the instantaneous droplet shape before impact and (e) the droplet shape after spreading on a thin film of air.

forces that cause droplet deformation, e.g., the inertia-capillary regime. As the thinning develops exponentially fast, beyond a critical strain rate, the polymers experience a coil-stretch transition regime where the extensional viscosity of the droplet increases by several orders of magnitude [37–39]. The viscosity increase then delays the pinch off and slows the thinning process as the elastic effects grow increasingly important, i.e., the elasto-capillary regime. We choose the start of the elasto-capillary regime as time $t = 0$ in Fig. 2.

Using the dripping-onto-substrate method described in Ref. [38], the relaxation time varies at least an order of magnitude between $\tau_E \approx 0.1$ and 6.2 ms as calculated by the Entov and Hinch theory [40], $R(t)/R_0 \approx [G/R_0/(2\gamma)]^{1/3} \exp[-t/(3\tau_E)]$, where $R(t)$ is the radius of the droplet neck, R_0 the initial thread radius, and G the elastic modulus. An exponential fitting of the data shown in Fig. 2, during the elasto-capillary regime (e.g., $t > 0$) gives the measured τ_E without knowing the prefactor.

III. RESULTS

Assuming negligible energy dissipation during the inversion, the precontact energy is converted to the deformation of the droplet, which eventually comes to near rest as impact is arrested. In an impact experiment, a spreading droplet forms capillary waves around the surface during the spreading phase [Fig. 3(a)]. Renardy *et al.* identified that the capillary waves cause the droplet to form a staircase-like structure [Fig. 3(a)] during spreading for We > 2 [41]. As the capillary waves propagate in time, at a critical time [e.g., 3.5 ms in Fig. 3(b)], the top surface inverts and forms a toroidal shape, similar to a "dry spot" as in Ref. [41]. We directly measure the top surface velocity, $dH/dt = U_\mathrm{T}$, where H is the distance between the top surface of the droplet and the substrate [blue arrow in Fig. 3(a)]. A vertically oriented laser sheet illuminated a cross section of the droplet, and we measured $|U_\mathrm{T}|$ to vary between 1 and 10 m/s [see Fig. 3(c)]. The top surface velocity is the same magnitude as the impact velocity in Fig. 3(b) at early times $t \approx 0 - 3\,\mathrm{ms}$ (e.g., droplet spreading) but diverges sharply around 4 ms. The sudden collapse of the top surface of the drop is caused by the focusing of the capillary waves at the apex of the droplet around 3 ms; we estimate that there is a displaced mass of liquid, $m \sim \pi \rho R_\mathrm{b}^2 H_\mathrm{b}$, where R_b is the radius and H_b the penetration depth of the inverted droplet top surface [see Fig. 3(e)]. The collapse of this cavity and the subsequent rising jet has been observed and modeled previously by the Rayleigh-Plesset equation [42,43].

We now provide order of magnitude estimates of the relevant quantities during the drop impact dynamics. First, the droplet motion toward the substrate is slowed by the ambient gas and completely stops at maximum spreading, which occurs at $t \approx 3\,\mathrm{ms}$ (Fig. 3). The critical condition for contact requires that the air must be purged beneath the droplet. The gas flow underneath the droplet is presumably viscous and at these speeds can be treated as incompressible [44], where at maximum spreading, the change in the minimum air film thickness is small (e.g., $dh/dt \approx 0$); thus the change in velocity of the gas caused by the bulk droplet motion is also negligibly small. Using a lubrication approximation for a channel flow, an estimate for the gas pressure under the droplet scales as $P_\mathrm{g} \sim \mu_\mathrm{g} u_\mathrm{g} R_\mathrm{b}/h^2$, where μ_g is the dynamic viscosity of the gas and u_g is the velocity of the gas. However, during the collapse of the top surface, the liquid near the droplet center is accelerated radially outward such that the liquid flow u_l induces a gas flow of similar magnitude (e.g., $u_\mathrm{l} \approx u_\mathrm{g}$). The radial gas flow is justified by taking into account the characteristic timescale of the flow induced by the collapse of the top surface, which scales as $t_\mathrm{T} \sim H_\mathrm{b}/U_\mathrm{T}$; the viscous diffusion timescale in the gas is $t_\mathrm{g} \sim h^2/\nu_\mathrm{g}$, where ν_g is the kinematic viscosity of the gas. Taking typical values of $t_\mathrm{T} \approx 5 \times 10^{-4}\,\mathrm{s}$ and $t_\mathrm{g} \approx 7 \times 10^{-8}\,\mathrm{s}$, the ratio $t_\mathrm{g}/t_\mathrm{T} \ll 1$. Taking the typical experimental values of $u_\mathrm{g} \approx 0.15\,\mathrm{m/s}$, $\mu_\mathrm{g} \approx 1.8 \times 10^{-5}\,\mathrm{mPa \cdot s}$, and the gas film thickness near the center to scale as $h \sim 10^{-6}\,\mathrm{m}$ [19], the gas pressure has magnitude $P_\mathrm{g} = O(100\,\mathrm{Pa})$. The collapse of the top surface induces fluid motion near the center of the droplet where the droplet inertia scales as $P_\mathrm{d} \sim \rho U_\mathrm{T}^2$, where $P_\mathrm{d} = (1000\,\mathrm{Pa})$. In the absence of PEO, the droplet is expected to make contact at the center under these conditions. Motivated by our experimental observations, we suggest below that viscoelastic effects influence P_d to suppress the droplet contact with the film below.

To further document the dynamics, we detected the change in the air film shape (at a fixed time $t \approx 3\,\mathrm{ms}$) as a function of PEO concentration (see Fig. 4). The shapes of the air films for water and 10 ppm droplets impacting the surface are similar, whereas beyond 10 ppm, the air film has significantly greater slopes radially outward (e.g., the radial reach of the 200 ppm droplets are nearly half as extended as the water droplets). The truncated extension of the air film close to the oil film surface shows that the air film shape significantly changes with increasing polymer concentration. A We ≈ 9 was observed to be the highest value for which a water droplet may sustain an air film through maximal spreading (e.g., $t \approx 3\,\mathrm{ms}$) and highlights the differences in the air film profile across PEO concentrations. The details of how the air film thicknesses were determined can be found in the Supplemental Material [36].

We hypothesize that the dynamical effect of polymer additives is related to high extension rates in the liquid associated with the collapse of the top surface. Based on the results in Fig. 4, the critical concentration at which the dynamics change occurs for polymer concentrations of magnitude 10 ppm. We now focus on the fluid movement in the droplet during the spreading phase. Performing PTV, the data for polystyrene particles (10–22 μm in diameter) moving in both the 200 ppm droplet and a water drop at We ≈ 6 are shown in Fig. 5; there is a clear increase in the average strain rate for water drops induced by the inversion of the top surface of the droplet. Between 4 and 4.5 ms, t_T is similar to the temporal resolution of the camera, and thus the actual strain rate in the water droplet is unknown during the collapse of the top surface. Nevertheless, in the PEO droplet, the strain rate plateaued rapidly, and the maximum strain rate in the viscoelastic droplet never overcomes that of

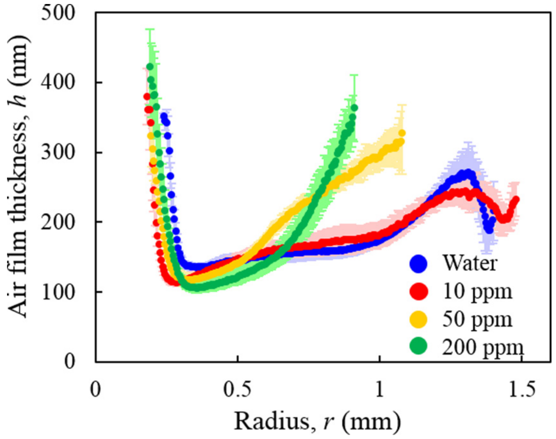

FIG. 4. Air film shapes for various PEO concentrations at t ≈ 3 ms from impact using TIRM for We ≈ 9. The error bars were obtained from three experiments.

the pure water droplet, consistent with the viscoelastic nature of the PEO droplet. We also note that in the PEO droplet, the extensional viscosity increases beyond a critical strain rate $\dot{\varepsilon} \approx 1/(2\tau_E)$, where there is an order of magnitude increase in the extensional viscosity due to the coil-stretch transition [45]. For 200 ppm droplets, $\tau_E \approx 4.2$ ms and thus $\dot{\varepsilon} \approx 120\ \mathrm{s}^{-1}$. According to the results in Fig. 5, the strain rates experienced by the droplet are $\dot{\varepsilon} > 120\ \mathrm{s}^{-1}$, and thus according to the FENE-P model [46,47] (see Supplemental Material [36]) we expect about a four orders of magnitude increase in the extensional viscosity of the droplet. We hypothesize that such a large increase in the extensional viscosity near the droplet center should damp the motion of the inverting droplet top surface in the z direction as well as resist deformation of the lower surface, both of which serve to inhibit contact with the surface below.

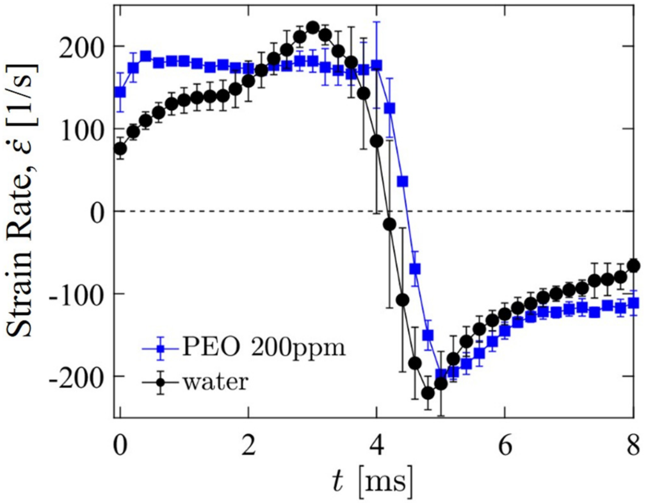

FIG. 5. Particle-tracking velocimetry (PTV) data showing the strain rate as a function of time for 200 ppm and water droplets for We ≈ 6. The time $t = 0$ is set as the beginning of the apparent impact with the surface and the start of the spreading phase of the droplet. The error bars were obtained from three experiments.

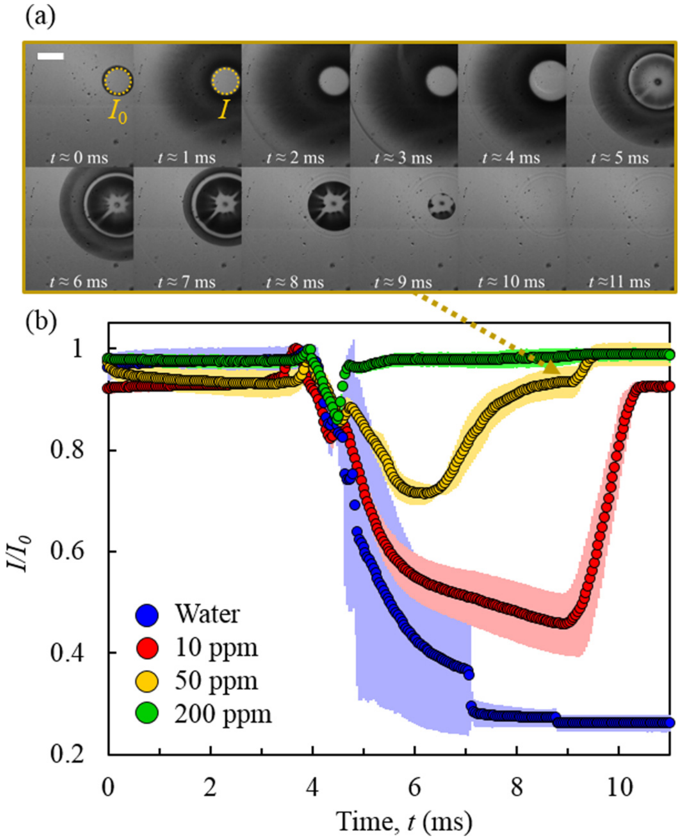

FIG. 6. (a) The TIRM image sequence of a droplet with 50 ppm PEO. (b) The change in the averaged normalized intensity (across five separate droplet impacts, where the shaded areas are the error bars of one standard deviation), I/I_0, at the droplet dimple center as a function of time for various PEO concentrations for We ≈ 9. The dotted arrow connects the TIRM image sequence to the processed data where I_0 is the average grayscale intensity at $t = 0$ and I is the average grayscale intensity for each sequential frame. The scale bar represents 0.5 mm.

We next explore the extent of the droplet impact-induced air film deformation at the droplet center using TIRM to provide evidence for the inhibition of the top surface inversion. In each droplet impact experiment, there exists a pocket of air or a dimple caused by the sudden pressure increase underneath the droplet, which grows large enough to deform the liquid droplet. The dimple height is an order of magnitude larger than the surrounding air film, which shows up as a bright circular area in the TIRM imaging [Fig. 6(a)] since the dimple is typically measured to be $O(1\ \mu\text{m})$ [16,19,48,49]. The normalized average intensity change in the dimple area is marked by the dotted circle in Fig. 6(a), where $t = 0$ is set as the initial time the dimple is observed in the TIRM setup. Moreover, I is the grayscale intensity of each frame and I_0 is the average grayscale intensity. For the case of water droplets, contact is made at $I/I_0 \lesssim 0.30$ for times between ≈4.5 ms and ≈7 ms, always at the center of the droplet, and thus always at the dimple [19]. However, with increasing polymer concentration beyond 10 ppm, the air in the dimple is sustained, e.g., the air film does not rupture, so that the droplet bounces—although the dimple is severely inverted and deformed. For experiments with 200 ppm, there is minimal perturbation of the dimple (e.g., $I/I_0 \gtrsim 0.85$), and thus we find direct experimental evidence for the prevention of the inversion of the top surface of the droplet.

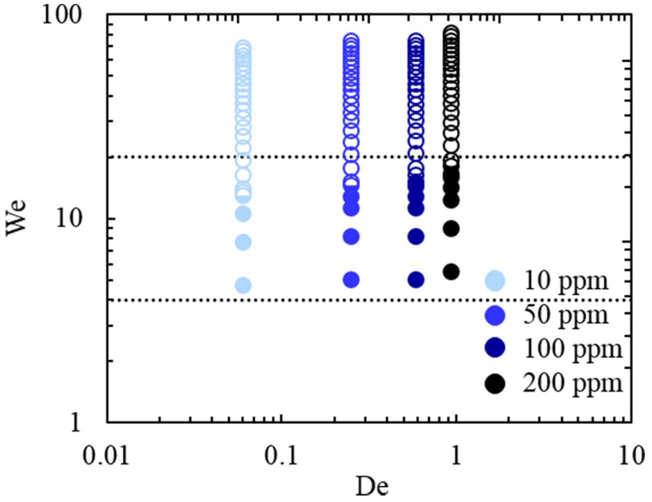

FIG. 7. Phase diagram for droplet bouncing. The dotted lines indicate the inertia-capillary dominant regime for air film failure for pure water droplets. Beyond $\mathrm{We} > 20$, the contact is initiated by disjoining pressure [19]. Empty symbols represent no bouncing, and solid symbols represent droplet bouncing for >80% of the tests. Half-filled symbols represent <50% of the droplets bounced. At least 100 impact tests were conducted for the solid symbols and the transitional data points below $\mathrm{We} < 20$.

We also investigated the range of the droplet bouncing for the various polymer concentrations. A phase diagram is outlined by the We and Deborah number, De, in Fig. 7, where $\mathrm{De} = \tau_\mathrm{E}/\tau_\mathrm{R}$, and we have defined the Rayleigh timescale, $\tau_\mathrm{R} = \sqrt{\rho (D_0/2)^3/\gamma}$, which describes the oscillation period of the droplets [50] and thus is utilized as the natural characteristic timescale for the dynamics. The transition from bouncing (solid) to no bouncing (open) for all of the polymer concentrations between 10 and 200 ppm is shown in Fig. 7. Droplets with different polymer concentrations are able to bounce beyond the inertia-capillary limit of pure water droplets (i.e., $\mathrm{We} \approx 4$) but cannot overcome the disjoining pressure dominant regime, where contact is made with the substrate spontaneously (i.e., $\mathrm{We} > 20$) [19]. The inertia-capillary limit and the disjoining pressure dominant regimes are marked by dotted lines in Fig. 7. There is a clear trend for the We as a function of De (i.e., PEO concentration) at which the bouncing ceases; with an increase in the polymer concentration, the bouncing threshold increases. There is nearly a 50% increase in the critical We for bouncing from 10 ppm to 200 ppm, while there is nearly a 17-fold increase in the extensional relaxation time ($\tau_\mathrm{E} \approx 0.25\,\mathrm{ms}$ to 4.2 ms). We also note that near the critical threshold for bouncing, the probability of bouncing over 100 droplet impact tests significantly drops below 50%. The existence of the probability of bouncing may be suggestive of the influence of external factors such as relative humidity and capillary waves generated at the droplet bottom during the collapse of the top surface, as well as the variability of droplet oscillations prior to impact, which are useful topics for future studies. Notably, the trend of increasing critical We for bouncing with an increase in the PEO concentration is present yet weak. Moreover, the trend is not easily quantifiable because the relationship among the air film underneath the droplet, extensional relaxation time in the dilute PEO-laden droplets, and the surface tension and viscosity of the droplet all have contributing influences to the dynamics, where the interplay of such variables is beyond the scope of this study.

IV. CONCLUSION

Herein we reported that for droplets impacting a substrate coated with a thin liquid film an increase in the dilute polymer concentration inhibited droplet-substrate contact under ambient temperatures. The nearly spherical geometry of the droplet provides a natural means by which capillary waves propagate, focus, and eventually invert the droplet surface to make contact with the substrate. Direct measurements of the air film underneath the droplet showed that the increase in polymer concentration in the droplet prevented the top surface inversion from puncturing the air film, which we attribute to damping and to the energy dissipated by the large extensional viscosity increase localized at the center of the droplet. We have justified the extensional viscosity increase by observing the large strain rates at the droplet center as measured using PTV. In summary, the extensional effects for dilute polymeric droplets cannot simply be ignored but play an important role in droplet deposition scenarios.

ACKNOWLEDGMENT

This research was partially supported by the NSF through Princeton University's Materials Research Science and Engineering Center DMR-1420541 and the Center for Chemomechanical Assembly (CCI-1740630).

[1] X. Zhao, H. Cui, Y. Wang, C. Sun, B. Cui, and Z. Zeng, Development strategies and prospects of nano-based smart pesticide formulation, J. Agric. Food Chem. **66**, 6504 (2018).

[2] E. Tekin, P. J. Smith, and U. S. Schubert, Inkjet printing as a deposition and patterning tool for polymers and inorganic particles, Soft Matter **4**, 703 (2008).

[3] K. Sun, P. Zhang, C. K. Law, and T. Wang, Collision Dynamics and Internal Mixing of Droplets of Non-Newtonian Liquids, Phys. Rev. Appl. **4**, 054013 (2015).

[4] S. V. Ravikumar, J. M. Jha, A. M. Tiara, S. K. Pal, and S. Chakraborty, Experimental investigation of air-atomized spray with aqueous polymer additive for high heat flux applications, Int. J. Heat Mass Transfer **72**, 362 (2014).

[5] G. Finotello, R. F. Kooiman, J. T. Padding, K. A. Buist, A. Jongsma, F. Innings, and J. A. M. Kuipers, The dynamics of milk droplet–droplet collisions, Exp. Fluids **59**, 17 (2017).

[6] A. L. Yarin, Drop impact dynamics: Splashing, spreading, receding, bouncing, Ann. Rev. Fluid Mech. **38**, 159 (2006).

[7] C. Josserand and S. T. Thoroddsen, Drop impact on a solid surface, Ann. Rev. Fluid Mech. **48**, 365 (2016).

[8] L. Xu, W. W. Zhang, and S. R. Nagel, Drop Splashing on a Dry Smooth Surface, Phys. Rev. Lett. **94**, 184505 (2005).

[9] Y. Wang, D. Minh, and G. Amberg, Dynamic wetting of viscoelastic droplets, Phys. Rev. E **92**, 043002 (2015).

[10] V. Bergeron, D. Bonn, J. Y. Martin, and L. Vovelle, Controlling droplet deposition with polymer additives, Nature (London) **405**, 772 (2000).

[11] D. Bartolo, A. Boudaoud, G. Narcy, and D. Bonn, Dynamics of Non-Newtonian Droplets, Phys. Rev. Lett. **99**, 174502 (2007).

[12] M. I. Smith and V. Bertola, Effect of Polymer Additives on the Wetting of Impacting Droplets, Phys. Rev. Lett. **104**, 154502 (2010).

[13] M. I. Smith and J. S. Sharp, Origin of contact line forces during the retraction of dilute polymer solution drops, Langmuir **30**, 5455 (2014).

[14] V. Bertola, Effect of polymer concentration on the dynamics of dilute polymer solution drops impacting on heated surfaces in the Leidenfrost regime, Exp. Therm. Fluid Sci. **52**, 259 (2014).

[15] W. Bouwhuis, R. C. A. van der Veen, T. Tran, D. L. Keij, K. G. Winkels, I. R. Peters, D. van der Meer, C. Sun, J. H. Snoeijer, and D. Lohse, Maximal Air Bubble Entrainment at Liquid-Drop Impact, Phys. Rev. Lett. **109**, 264501 (2012).

[16] J. de Ruiter, J. M. Oh, D. van den Ende, and F. Mugele, Dynamics of Collapse of Air Films in Drop Impact, Phys. Rev. Lett. **108**, 074505 (2012).

[17] J. S. Lee, B. M. Weon, J. H. Je, and K. Fezzaa, How Does an Air Film Evolve Into a Bubble During Drop Impact?, Phys. Rev. Lett. **109**, 204501 (2012).

[18] S. T. Thoroddsen, T. G. Etoh, K. Takehara, N. Ootsuka, and Y. Hatsuki, The air bubble entrapped under a drop impacting on a solid surface, J. Fluid Mech. **545**, 203 (2005).

[19] M. Pack, H. Hu, D. Kim, Z. Zheng, H. A. Stone, and Y. Sun, Failure mechanisms of air entrainment in drop impact on lubricated surfaces, Soft Matter **13**, 2402 (2017).

[20] J. d. Ruiter, F. Mugele, and D. van den Ende, Air cushioning in droplet impact. I. Dynamics of thin films studied by dual wavelength reflection interference microscopy, Phys. Fluids **27**, 012104 (2015).

[21] J. M. Kolinski, L. Mahadevan, and S. M. Rubinstein, Lift-Off Instability During the Impact of a Drop on a Solid Surface, Phys. Rev. Lett. **112**, 134501 (2014).

[22] J. de Ruiter, R. Lagraauw, D. van den Ende, and F. Mugele, Wettability-independent bouncing on flat surfaces mediated by thin air films, Nat. Phys. **11**, 48 (2014).

[23] J. de Ruiter, R. Lagraauw, F. Mugele, and D. van den Ende, Bouncing on thin air: How squeeze forces in the air film during non-wetting droplet bouncing lead to momentum transfer and dissipation, J. Fluid Mech. **776**, 531 (2015).

[24] C. Hao, J. Li, Y. Liu, X. Zhou, Y. Liu, R. Liu, L. Che, W. Zhou, D. Sun, L. Li, L. Xu, and Z. Wang, Superhydrophobic-like tunable droplet bouncing on slippery liquid interfaces, Nat. Commun. **6**, 7986 (2015).

[25] L. Chen, J. Wu, Z. Li, and S. Yao, Evolution of entrapped air under bouncing droplets on viscoelastic surfaces, Colloids Surf. A **384**, 726 (2011).

[26] M. Pack, P. Kaneelil, H. Kim, and Y. Sun, Contact line instability caused by air rim formation under nonsplashing droplets, Langmuir **34**, 4962 (2018).

[27] J. M. López-Herrera, S. Popinet, and A. A. Castrejón-Pita, An adaptive solver for viscoelastic incompressible two-phase problems applied to the study of the splashing of weakly viscoelastic droplets, J. Non-Newtonian Fluid Mech. **264**, 144 (2019).

[28] G. Finotello, S. De, J. C. R. Vrouwenvelder, J. T. Padding, K. A. Buist, A. Jongsma, F. Innings, and J. A. M. Kuipers, Experimental investigation of non-Newtonian droplet collisions: The role of extensional viscosity, Exp. Fluids **59**, 113 (2018).

[29] D. Izbassarov and M. Muradoglu, Effects of viscoelasticity on drop impact and spreading on a solid surface, Phys. Rev. Fluids **1**, 023302 (2016).

[30] H. K. Huh, S. Jung, K. W. Seo, and S. J. Lee, Role of polymer concentration and molecular weight on the rebounding behaviors of polymer solution droplet impacting on hydrophobic surfaces, Microfluid. Nanofluid. **18**, 1221 (2015).

[31] L. Chen, Y. Wang, X. Peng, Q. Zhu, and K. Zhang, Impact dynamics of aqueous polymer droplets on superhydrophobic surfaces, Macromolecules **51**, 7817 (2018).

[32] M. Guémas, Á. G. Marín, and D. Lohse, Drop impact experiments of non-Newtonian liquids on micro-structured surfaces, Soft Matter **8**, 10725 (2012).

[33] E. Q. Li, I. U. Vakarelski, and S. T. Thoroddsen, Probing the nanoscale: The first contact of an impacting drop, J. Fluid Mech. **785**, R2 (2015).

[34] J. M. Kolinski, S. M. Rubinstein, S. Mandre, M. P. Brenner, D. A. Weitz, and L. Mahadevan, Skating on a Film of Air: Drops Impacting on a Surface, Phys. Rev. Lett. **108**, 074503 (2012).

[35] M. Shirota, M. A. J. van Limbeek, D. Lohse, and C. Sun, Measuring thin films using quantitative frustrated total internal reflection (FTIR), Eur. Phys. J. E **40**, 54 (2017).

[36] See Supplemental Material at http://link.aps.org/supplemental/10.1103/PhysRevFluids.4.123603 for the rheology of the droplets, particle tracking velocimetry, and the determination of the air film thickness.

[37] S. L. Anna and G. H. McKinley, Elasto-capillary thinning and breakup of model elastic liquids, J. Rheol. **45**, 115 (2001).

[38] J. Dinic, Y. Zhang, L. N. Jimenez, and V. Sharma, Extensional relaxation times of dilute, aqueous polymer solutions, ACS Macro Lett. **4**, 804 (2015).

[39] E. Turkoz, A. Perazzo, H. Kim, H. A. Stone, and C. B. Arnold, Impulsively Induced Jets from Viscoelastic Films for High-Resolution Printing, Phys. Rev. Lett. **120**, 074501 (2018).

[40] V. M. Entov and E. J. Hinch, Effect of a spectrum of relaxation times on the capillary thinning of a filament of elastic liquid, J. Non-Newtonian Fluid Mech. **72**, 31 (1997).

[41] Y. Renardy, S. Popinet, L. Duchemin, M. Renardy, S. Zaleski, C. Josserand, M. A. Drumright-Clarke, D. Richard, C. Clanet, and D. Quere, Pyramidal and toroidal water drops after impact on a solid surface, J. Fluid Mech. **484**, 69 (2003).

[42] L. Chen, L. Li, Z. Li, and K. Zhang, Submillimeter-sized bubble entrapment and a high-speed jet emission during droplet impact on solid surfaces, Langmuir **33**, 7225 (2017).

[43] D. Bartolo, C. Josserand, and D. Bonn, Singular Jets and Bubbles in Drop Impact, Phys. Rev. Lett. **96**, 124501 (2006).

[44] S. Mandre, M. Mani, and M. P. Brenner, Precursors to Splashing of Liquid Droplets on a Solid Surface, Phys. Rev. Lett. **102**, 134502 (2009).

[45] Y. Amarouchene, D. Bonn, J. Meunier, and H. Kellay, Inhibition of the Finite-Time Singularity During Droplet Fission of a Polymeric Fluid, Phys. Rev. Lett. **86**, 3558 (2001).

[46] A. Lindner, J. Vermant, and D. Bonn, How to obtain the elongational viscosity of dilute polymer solutions?, Physica A **319**, 125 (2003).

[47] B. Keshavarz and G. H. McKinley, Micro-scale extensional rheometry using hyperbolic converging/diverging channels and jet breakup, Biomicrofluidics **10**, 043502 (2016).

[48] R. C. A. van der Veen, T. Tran, D. Lohse, and C. Sun, Direct measurements of air layer profiles under impacting droplets using high-speed color interferometry, Phys. Rev. E **85**, 026315 (2012).

[49] K. Langley, E. Q. Li, and S. T. Thoroddsen, Impact of ultra-viscous drops: Air-film gliding and extreme wetting, J. Fluid Mech. **813**, 647 (2017).

[50] C. Clanet, C. Beguin, D. Richard, and D. Quere, Maximal deformation of an impacting drop, J. Fluid Mech. **517**, 199 (2004).